

Vision Transformer-based Multimodal Feature Fusion Network for Lymphoma
Segmentation on PET/CT Images

Huan Huang¹·Liheng Qiu²·Shenmiao Yang³·Longxi Li¹·Jiaofen Nan¹·Yanting Li¹·Chuang Han¹·Fubao Zhu^{1*}·Chen Zhao^{4*}·Weihua Zhou^{5,6}

¹ School of Computer Science and Technology, Zhengzhou University of Light Industry, Zhengzhou 450002, Henan, China

² Peking University Peoples' Hospital, Peking University Institute of Hematology, Beijing, China

³ Department of Nuclear Medicine, Peking University Peoples' Hospital, Beijing, China

⁴ Department of Computer Science, Kennesaw State University, Marietta, GA, USA

⁵ Department of Applied Computing, Michigan Technological University, Houghton, MI, USA

⁶ Center for Biocomputing and Digital Health, Institute of Computing and Cybersystems, and Health Research Institute, Michigan Technological University, Houghton, MI, USA

Huan Huang and Liheng Qiu contributed equally.

* Correspondence:

Fubao Zhu

Email address: fbzhu@zzuli.edu.cn

Mailing address: School of Computer Science and Technology, Zhengzhou University of Light Industry, Zhengzhou 450002, Henan, China

Chen Zhao

Email address: czhao4@kennesaw.edu

Mailing address: 680 Arntson Dr, Atrium BLDG, Marietta, GA 30060

Abstract

Background: Diffuse large B-cell lymphoma (DLBCL) segmentation is a challenge in medical image analysis. Traditional segmentation methods for lymphoma struggle with the complex patterns and the presence of DLBCL lesions.

Objective: We aim to develop an accurate method for lymphoma segmentation with 18F-Fluorodeoxyglucose positron emission tomography (PET) and computed tomography (CT) images.

Methods: Our lymphoma segmentation approach combines a vision transformer with dual encoders, adeptly fusing PET and CT data via multimodal cross-attention fusion (MMCAF) module. In this study, PET and CT data from 165 DLBCL patients were analyzed. A 5-fold cross-validation was employed to evaluate the performance and generalization ability of our method. Ground truths were annotated by experienced nuclear medicine experts. We calculated the total metabolic tumor volume (TMTV) and performed a statistical analysis on our results.

Results: The proposed method exhibited accurate performance in DLBCL lesion segmentation, achieving a Dice similarity coefficient of 0.9173 ± 0.0071 , a Hausdorff distance of 2.71 ± 0.25 mm, a sensitivity of 0.9462 ± 0.0223 , and a specificity of 0.9986 ± 0.0008 . Additionally, a Pearson correlation coefficient of 0.9030 ± 0.0179 and an R-square of 0.8586 ± 0.0173 were observed in TMTV when measured on manual annotation compared to our segmentation results.

Conclusion: This study highlights the advantages of MMCAF and vision transformer for lymphoma segmentation using PET and CT, offering great promise for computer-aided lymphoma diagnosis and treatment.

Keywords: deep learning, lymphoma, multimodal cross-attention, segmentation, transformer

1. Introduction

Diffuse large B-cell lymphoma (DLBCL) is a common subtype of non-Hodgkin lymphoma¹. Two thirds of patients with DLBCL can be cured by R-CHOP like chemoimmunotherapy². In clinical practice, 18F-Fluorodeoxyglucose (FDG) positron emission tomography and computed tomography (PET/CT) are employed for DLBCL staging and response assessment^{3,4}. The integration of both CT and PET imaging is important for lymphoma segmentation, as it allows for a comprehensive evaluation that combines metabolic activity from PET with anatomical information provided by CT⁵.

Total metabolic tumor volume (TMTV) is a prognostic biomarker for DLBCL^{6,7}. Accurate lymphoma segmentation is important for determining TMTV. However, manual delineation of lymphoma is time-consuming and subjective. Advances in deep learning have led to automated methods, offering consistency and precision in segmentation^{8,9}.

Traditional methods of lymphoma segmentation, such as thresholding and region growing, have limitations. Thresholding is straightforward but lacks adaptability¹⁰, as it cannot cope with the varying image conditions due to the similar gray values of lymphoma and normal tissue. Region growing heavily depends on seed points¹¹. It requires appropriate selection of initial seed points and growing criteria to deal with the diverse shapes and sizes of lymphoma. Nevertheless, there has been notable progress in lymphoma segmentation through the application of deep learning methods. The Dense X-Net proposed by Li et al.¹² showed good performance in segmentation of lymphoma with PET/CT, achieving a Dice similarity coefficient (DSC) of 0.728. Blanc-Durand et al.⁷ employed convolutional neural networks (CNN) for segmentation of DLBCL lesions with PET/CT, achieving a DSC of 0.73. Huang et al.^{13,14} attained high accuracy in segmentation of lymphoma. Although these methods had impressive results, they did not fully utilize the complementary information of PET/CT multimodal data^{8,15}. Furthermore, due to the limitation of the receptive field of CNN, they faced significant challenges in capturing both the global information and local information in small lesion areas simultaneously^{16,17}.

This study introduces a new lymphoma segmentation method based on vision transformer and multimodal feature fusion. It leverages PET and CT images through a multimodal cross-attention fusion (MMCAF) model. The transformer structure enables the model to capture global information^{18,19} better and addresses the limitations of traditional CNNs in establishing long-range dependencies. This study not only focuses on the automatic segmentation of lymphoma images but also extends to the calculation of TMTV. The contributions of this study are as follows:

- 1) Multimodal feature extraction:** Vision transformer is employed to enhance our model's ability for capturing global information. Additionally, a dual encoder is employed to thoroughly extract features from both PET and CT. These techniques enable us to effectively utilize all available information.
- 2) Multimodal feature fusion:** Our method combines the complementary information from PET and CT images through MMCAF, thereby improving the accuracy and reliability of lymphoma segmentation.

- 3) **Applying lymphoma segmentation to TMTV calculation:** The study focuses on both lymphoma segmentation and TMTV calculation, which are crucial for assessing treatment effectiveness and prognosis.

2. Method and Material

2.1 Dataset

This study involved 165 PET/CT scan datasets from patients clinically diagnosed with DLBCL. All data were provided by Peking University Peoples' Hospital. The PET/CT scanning data were acquired using Discovery VCT PET/CT scanner (GE Healthcare, Milwaukee, Wisconsin, USA), and image reconstruction was performed using the Ordered Subset Expectation Maximization method. PET images were manually segmented by experienced nuclear medicine experts to ensure the accuracy. PET images were acquired one hour after the intravenous injection of 18F-FDG to obtain optimal metabolic activity information.

The size of CT images is 512×512, with a pixel size of 0.98 mm×0.98 mm per pixel. While the size of PET images is 128×128, with a pixel size of 5.47 mm×5.47 mm per pixel. Both PET and CT images underwent reconstruction using an identical number of slices, and the slice thickness is 3.27 mm.

2.2 Data preprocessing

Rigid-body registration is a standard operation in the segmentation of PET/CT^{20,21}, to align PET and CT volumes in the same coordinate space.^{20, 21} We upsampled the PET image size to 256×256 using bicubic interpolation, and CT images were downsampled to the same size.

According to the clinician's suggestion, the window width of the CT images was adjusted to 400 Hounsfield unit (HU), and the window level was adjusted to 40 HU²². We used Body Weight-Corrected Standard Uptake Value (SUV_{BW}) to normalize PET images, which is commonly used to semi-quantitatively evaluate the uptake level of FDG^{23, 24}, as defined in Eq. (1).

$$SUV_{BW} = \frac{RS \times PV + RI}{A \times e^{\frac{-0.693}{T_{1/2}} \times (t_1 - t_0)}} / (W \times 1000) \quad (1)$$

where PV represents the pixel value of PET slices, RS denotes the rescale slope of PET imaging, RI signifies the rescale intercept of PET imaging, A represents the total dose of the radioactive isotope for each patient, $T_{1/2}$ is the radioactive isotope half-life of 18F-FDG, t_0 is the start time of the radiopharmaceutical injection, t_1 is the image acquisition time, and W denotes the weight of the patient.

We used ResNet-152²⁵ as the backbone network and employed a pre-trained model to train a binary classifier for tumor slice detection. This classifier facilitated the identification of potential lymphoma-containing PET/CT image slices. Ultimately, we obtained 11,370 pairs of PET/CT slices, each comprising one PET slice and one CT slice.

2.3 Network architecture

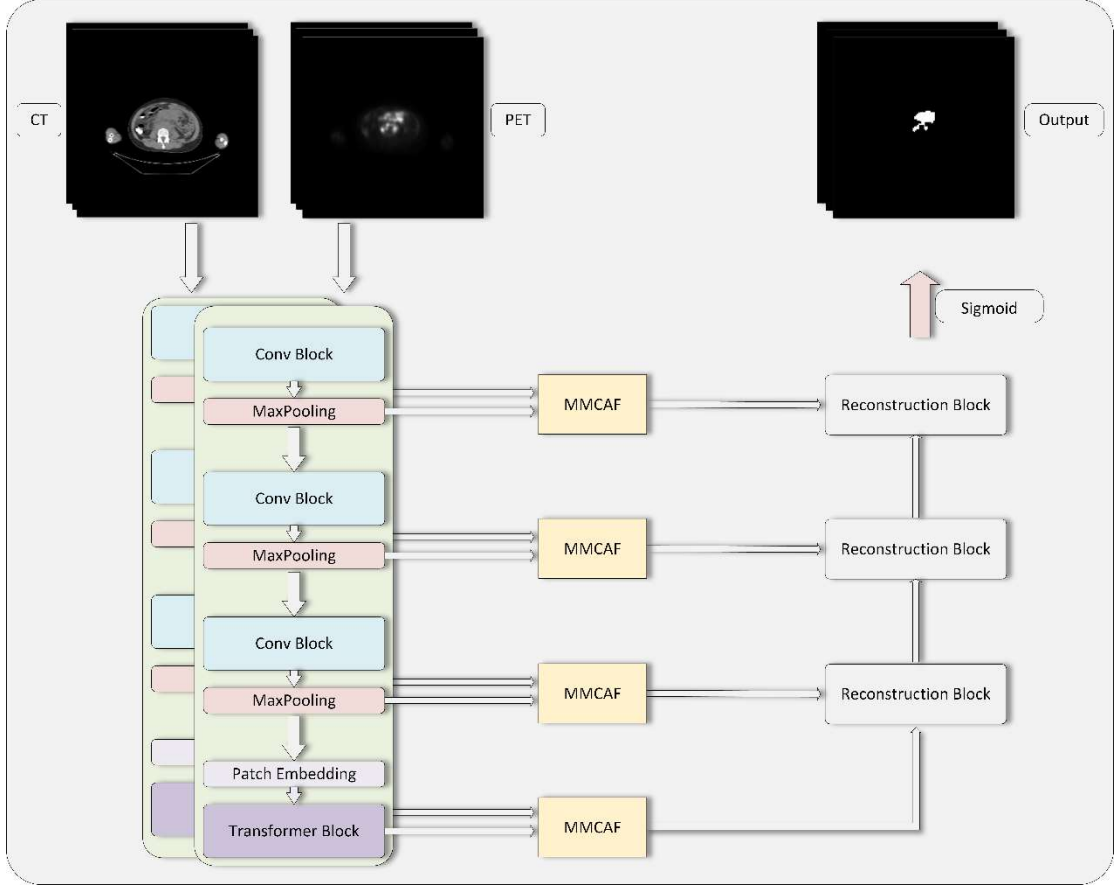


Fig. 1: The proposed network architecture, which has two identical encoders. The MMCAF component receives PET and CT features and integrates them through a multimodal cross attention mechanism. Following the reconstruction blocks, the Sigmoid function is applied to obtain the final segmentation result.

2.3.1 Encoders

Figure 1 presents the proposed network architecture, which consists of two encoder branches with identical structure for feature extraction from PET and CT images. Each encoder branch processes either PET or CT images and captures unique information from each modality.

$$F_i = \text{Maxpooling} \left(\text{ReLU} \left(\text{Normalize} \left(\text{Conv} \left(X_{input} \right) \right) \times 2 \right) \right) \quad (2)$$

As shown in Eq. (2), each encoder consists of blocks with convolution, normalization, and ReLU activation functions. Skip connections²⁵ and MaxPooling layers enhance features and reduce dimensions. The input is a two-dimensional pixel matrix image (denoted as X_{input}), where F_i is the output of the i -th MaxPooling operation after the convolutional blocks. Each convolutional block consists of two sets of convolutions, normalization, and ReLU operations, denoted by the “ $\times 2$ ” in the formula. Specifically, after the third convolutional block and MaxPooling operation, the output is F_3 . The next step involves feeding F_3 into the vision transformer²⁶ (ViT) module.

The ViT module converts convolutional feature maps into sequences, adds positional encoding information, and uses multiple transformer blocks to capture global context. Specifically, the ViT module partitions the input feature maps into uniform

patches. This can be represented as:

$$X = [x^1 E, x^2 E, \dots, x^N E] + E_{pos} \quad (3)$$

where X is a patch sequence with dimension $M \times N$, where M is the number of patches and N is a hyperparameter adjustable based on the model and dataset. In Eq. (3), x^i is the i -th patch, E is a linear projection matrix with dimension $(P^2 \times C) \times N$, where P is the patch size and C is the channel of the input image. E_{pos} is the positional encoding matrix with dimensions $M \times N$. E_{pos} adds position information for each patch, enabling the transformer to distinguish different patches. Both E_{pos} and E are learned parameters which can be updated through backpropagation using gradient descent.

After obtaining the transformed input, we feed it into multiple transformer blocks, each consisting of a multi-head self-attention layer and a multi-layer perceptron layer. As shown in Eq. (4), LN represents layer normalization, MSA represents multi-head self-attention and MLP represents multi-layer perceptron. Finally, we obtain the output of the encoder, denoted as *output*, which contains a high-level abstract representation of the input image.

$$output = LN(MLP(LN(MSA(LN(X)))))) \quad (4)$$

2.3.2 Feature fusion

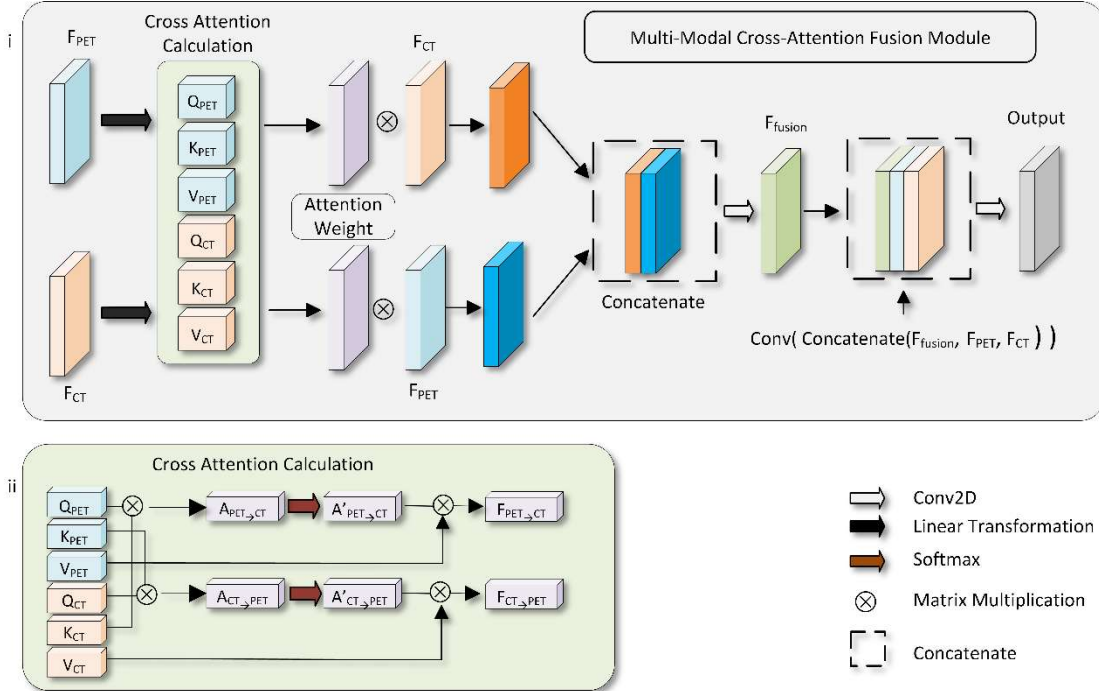


Fig. 2: The feature fusion module, (i) represents the architecture of MMCAF, (ii) is the process of the cross-attention mechanism, F_{PET} and F_{CT} represent the intermediate feature map of the two modalities of data respectively.

In the feature fusion module, we employ a multimodal cross attention mechanism²⁷. For each modality, feature maps are denoted as F_{modal} . We generate Query (denoted as Q_{modal}), Key (denoted as K_{modal}), and Value (denoted as V_{modal}) matrices from F_{modal} . This is achieved by multiplying F_{modal} with weight matrices W_Q , W_K , and W_V , show in Eq. (5) and Eq. (6).

$$Q_{PET}, K_{PET}, V_{PET} = F_{PET} \otimes (W_{Q(PET)}, W_{K(PET)}, W_{V(PET)}) \quad (5)$$

$$Q_{CT}, K_{CT}, V_{CT} = F_{CT} \otimes (W_{Q(CT)}, W_{K(CT)}, W_{V(CT)}) \quad (6)$$

As shown in Figure 2 (ii), the cross-attention scores are computed between the PET features (F_{PET}) and the CT features (F_{CT}) through a dot product operation between Q_{PET} and K_{CT} , denoted as $A_{PET \rightarrow CT}$. Similarly, $A_{CT \rightarrow PET}$ is generated by Q_{CT} and K_{PET} and these operations effectively measure the similarity between PET and CT features. These attention scores are then transformed into weights via a SoftMax operation, specifically representing the focus of F_{PET} on F_{CT} which is denoted as $A'_{PET \rightarrow CT}$. Similarly, $A'_{CT \rightarrow PET}$ indicates the focus of F_{CT} on F_{PET} . The SoftMax operation normalizes the attention scores to create a probability distribution ranging between 0 and 1, ensuring the interpretability and stability of the attention mechanism. Then $A'_{PET \rightarrow CT}$ and $A'_{CT \rightarrow PET}$ are applied to V_{CT} and V_{PET} , producing the attention output from F_{PET} to F_{CT} and F_{CT} to F_{PET} , which are denoted as $F_{PET \rightarrow CT}$ and $F_{CT \rightarrow PET}$, respectively. The $F_{CT \rightarrow PET}$ and $F_{PET \rightarrow CT}$ indicate the specific areas within one modality that are significant for the other. Mathematically, the cross attention is defined in EQ. (7) and EQ. (8):

$$F_{PET \rightarrow CT} = Softmax \left(\frac{Q_{PET} \otimes K_{CT}}{\sqrt{d_k}} \right) \otimes V_{CT} \quad (7)$$

$$F_{CT \rightarrow PET} = Softmax \left(\frac{Q_{CT} \otimes K_{PET}}{\sqrt{d_k}} \right) \otimes V_{PET} \quad (8)$$

where d_k is a scaling factor, that is set to the dimension of K . This process prevents values from becoming excessively large or small, resulting in a smoother and more easily optimized output from the SoftMax function.

To integrate information from both modalities, the attention output $F_{PET \rightarrow CT}$ is weighted with F_{CT} features, resulting in the fusion feature $F'_{PET \rightarrow CT}$. Similarly, the fusion feature $F'_{CT \rightarrow PET}$ is obtained, as shown in Eq. (9) and Eq. (10). This design allows each modality to concentrate on crucial information from another modality and acquire the cross-modality information.

$$F'_{PET \rightarrow CT} = F_{PET \rightarrow CT} \otimes F_{CT} \quad (9)$$

$$F'_{CT \rightarrow PET} = F_{CT \rightarrow PET} \otimes F_{PET} \quad (10)$$

To minimize information loss, the fusion features $F'_{PET \rightarrow CT}$ and $F'_{CT \rightarrow PET}$ are concatenated. These concatenated features are then processed through a convolution (Conv) operation to generate the multimodal fusion feature F_{fusion} , as shown in Eq. (11):

$$F_{fusion} = Conv(F'_{CT \rightarrow PET} \oplus F'_{PET \rightarrow CT}) \quad (11)$$

where \oplus is the concatenation operator.

Ultimately, the multimodal fusion feature F_{fusion} is concatenated with the original features F_{PET} and F_{CT} . This combined feature is then processed through a Conv operation to obtain the complete fusion feature, as shown in Eq. (12). This strategy

ensures comprehensive integration of complementary information from both modalities.

$$Output = Conv(F_{fusion} \oplus F_{PET} \oplus F_{CT}) \quad (12)$$

2.3.3 Decoder

The decoder of this network has three reconstruction blocks and a Sigmoid activation layer. Each reconstruction block upscales the output from the MMCAF module to match the original input's scale and reconstructs the regions of interest.

The reconstruction blocks share a uniform structural layout, which includes an upsampling layer followed by two convolution layers. The upsampling layer uses the nearest-neighbor interpolation technique, enlarging the feature map's size to keep the spatial scale consistent with the original input. The two subsequent convolution layers merge and optimize semantic information, producing high-dimensional feature maps. After processing through the reconstruction blocks, these features maps, pass through a final Sigmoid activation layer, resulting in the prediction map.

2.4 Segmentation evaluation criteria

We employ the following evaluation metrics to assess the segmentation model's performance:

Dice Similarity Coefficient (DSC): DSC is commonly used to measure segmentation accuracy, as shown in Eq. (13):

$$DSC = \frac{2 \times TP}{2 \times TP + FP + FN} \quad (13)$$

where TP (True Positives) represents the number of correctly classified positive samples, FP (False Positives) represents the number of misclassified positive samples, FN (False Negatives) represents the number of misclassified negative samples, and TN (True Negatives) represents the number of correctly classified negative samples.

Hausdorff Distance (HD): The HD is used to quantify segmentation accuracy and boundary matching, which is defined as follows:

$$HD = \max(\text{surface}(\text{set } A, \text{set } B), \text{surface}(\text{set } B, \text{set } A)) \quad (14)$$

where $\text{surface}(\text{set } A, \text{set } B)$ represents the distance from the predicted segmentation $\text{set } A$ to the ground truth segmentation $\text{set } B$, while $\text{surface}(\text{set } B, \text{set } A)$ represents the distance from the ground truth segmentation $\text{set } B$ to the predicted segmentation $\text{set } A$.

Sensitivity is calculated as follows:

$$Sensitivity = \frac{TP}{TP + FN} \quad (15)$$

Specificity is calculated as follows:

$$Specificity = \frac{TN}{TN + FP} \quad (16)$$

2.5 Implementation and experiments

We implemented the network using PyTorch 1.10²⁸. Training was conducted on an Ubuntu 16.04 server equipped with a Tesla V100 GPU. We used a batch size of 16 and trained each fold for 100 epochs. The ViT model parameters were configured as follows: the patch size was set to 16, the head number of multi-head attention

mechanism was 4, the layer number of MLP was 512, the number of transformer block was 8, and the dropout rate was 0.1. For optimization, we employed the Adam optimizer²⁹ with a dynamic learning rate. Initially, the learning rate was set to 0.001, β_1 and β_2 were set to 0.9 and 0.999 empirically. We employed binary cross-entropy loss to penalize the difference between the segmentation maps and the ground truth of lymphoma, as represented in Eq. (17).

$$L = -\frac{1}{N} \sum_{i=1}^N \left[y_i \cdot \log(p(y_i)) + (1 - y_i) \cdot \log(1 - p(y_i)) \right] \quad (17)$$

where N is the total number of pixels, y_i denotes the true labels (0 or 1), indicating whether a pixel belongs to the lymphoma region, and $p(y_i)$ represents the model's output probabilities.

We applied the 5-fold cross-validation to 11,370 PET/CT image pairs from 165 subjects. Each training set included PET/CT pairs from 132 subjects, and each test set included pairs from 33 subjects.

This study compared single-modal methods, such as U-Net³⁰ and Trans U-Net⁸. Furthermore, we also compared multimodal methods, such as hybrid learning, which replaced the transformer and MMCAF in our structure with concatenation and convolution operations. U-Net has a U-shaped network structure and skip connections that extract high-level semantic information and preserve spatial resolution. The Trans U-Net merges the self-attention mechanism of transformers with the U-Net architecture, utilizing unimodal images for lymphoma segmentation.

2.6 TMTV calculation

In this study, we used the lymphoma segmentation model (Section 2.3) to analyze PET/CT images for TMTV calculation. The computation of TMTV involved summing voxels within the predicted binarized masks³¹, which were generated by applying a thresholding method with a threshold of 0.5. Because the image size of PET was enhanced to 256×256, the voxel resolution was adjusted to 2.735 mm × 2.735 mm × 3.27 mm. Lesion area volumes were calculated using Eq. (18), where V_i is the volume of the lymphoma in i -th slice, and S is the total number of lesion slices.

$$TMTV = \sum_{i=1}^S V_i \quad (18)$$

To assess the accuracy of calculated TMTV (cTMTV) against ground truth TMTV (gtTMTV), we employed linear regression analysis and Pearson correlation coefficient to evaluate the model performance. Additionally, a paired t-test was employed to assess the statistical differences between the two methods. We also used the determination coefficient (R^2) to quantify the consistency between cTMTV and gtTMTV. Additionally, Bland Altman analysis evaluated the agreement between the two methods.

Consistent with the segmentation task, the remaining fold in five-fold cross-validation was used for independent testing of segmentation performance and TMTV computation.

3 Results

3.1 Segmentation results

Table1: Results of different methods in lymphoma segmentation.

Model	Data Type	DSC	HD (mm)	Sensitivity	Specificity
U-Net	□PET ✓CT	0.2977±0.1235	3.53±1.73	0.6126±0.0825	0.9713±0.0025
Trans U-Net	□PET ✓CT	0.3755±0.0987	3.42±1.25	0.6674±0.0642	0.9897±0.0028
U-Net	✓PET □CT	0.8415±0.0172	2.91±0.47	0.8353±0.0749	0.9954±0.0008
Hybrid Learning	✓PET ✓CT	0.8432±0.0135	2.88±0.62	0.8547±0.0468	0.9978±0.0014
Trans U-Net	✓PET □CT	0.8985±0.0083	2.75±0.31	0.9192±0.0239	0.980±0.0012
Ours	✓PET ✓CT	0.9173±0.0071	2.71±0.25	0.9462±0.0223	0.9986±0.0008

Table 1 demonstrates the result of different methods, as measured by DSC, HD, sensitivity, and specificity. The table encompasses a range of models that use single-modal input data, either CT or PET, as well as multimodal approaches that integrate both PET and CT data.

The method proposed in this study outperforms competing models across all performance metrics. Notably, the DSC of the proposed method is 0.9173 ± 0.0071 . The model also achieves a high sensitivity of 0.9462 ± 0.0223 , ensuring effective detection of lymphoma lesions, which is paramount for precise localization and subsequent diagnostic processes. Concurrently, the model maintains a high specificity of 0.9986 ± 0.0008 , indicating a robust ability to discriminate between pathological and normal tissues, which enhances the reliability of the segmentation results.

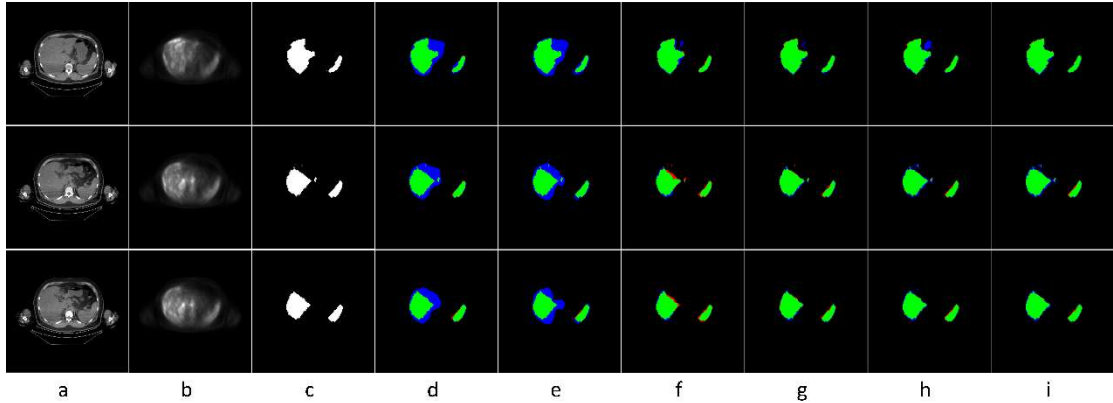


Fig. 3. Difference maps of segmentation results compared with ground truth. The green, red, and blue regions represent true positive, false negative, and false positive pixels, respectively. (a). CT images, (b). PET images, (c). ground truth. Difference maps generated by (d). U-Net with CT, (e). Trans U-Net with CT, (f). U-Net with PET, (g). Hybrid Learning, (h). Trans U-Net with PET, and (i). our method.

Figure 3 shows the results of different segmentation methods in difference maps. This comparison highlights the effectiveness of different approaches, especially in smaller lesion regions. The method that uses only CT data shows limited efficacy, while the method that uses PET data leads to significant improvement. The proposed model exhibits heightened sensitivity to lymphoma lesion boundaries, aligning closely with the ground truths and evidencing its precision in lymphoma lesion segmentation.

3.2 Computational complexity

We compared inference time, weight count, and total required Floating-Point Operations (FLOPs) for different methods. All tests were conducted on a workstation with an NVIDIA Tesla V100 GPU. As shown in Table 2, our method has the highest computational requirement among all methods. It also has the lowest inference efficiency and the largest weight size, which may consume more memory.

Table 2: Comparison of the computation complexity. The inference time (in milliseconds), number of weights, and the required total FLOPs are presented.

Model	Time (ms)	# Weights	FLOPs
U-Net	344.393	34.526 M	65.447 G
Trans U-Net	252.434	66.803 M	32.427 G
Hybrid Learning	252.434	11.860 M	22.077 G
Ours	5043.067	687.126 M	1.5503 T

3.3 Results of TMTV

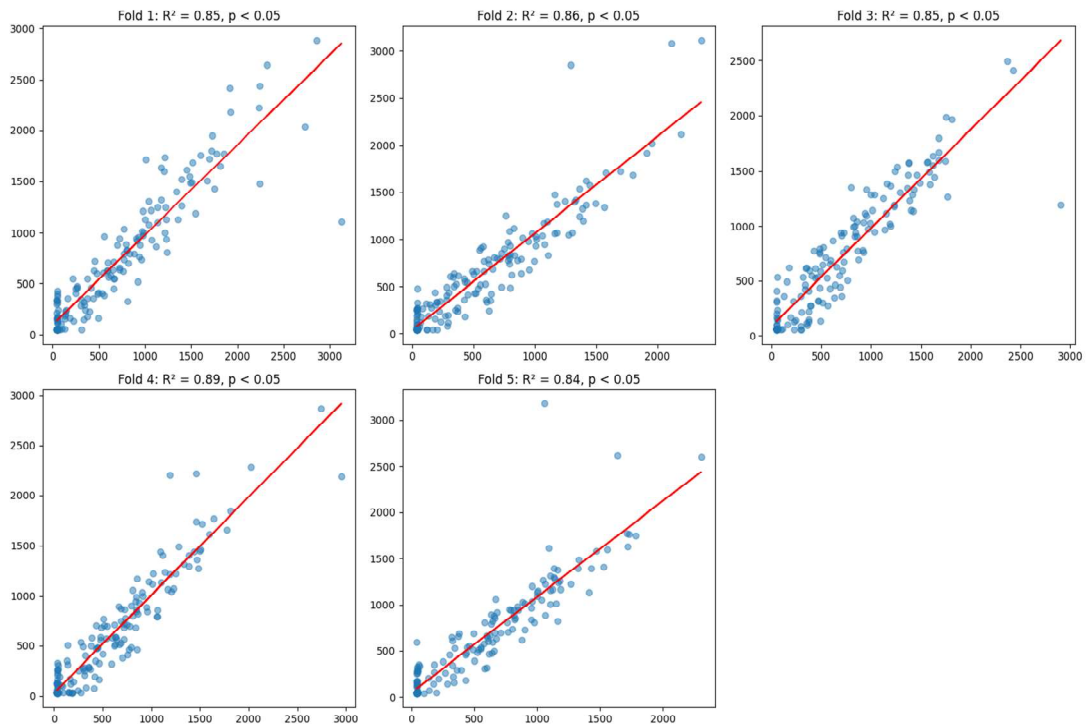


Fig. 4. Regression analyses between cTMTV and gtTMTV in the lymphoma patients of the test sets of each fold, and these analyses were performed using the five-fold cross-validation method.

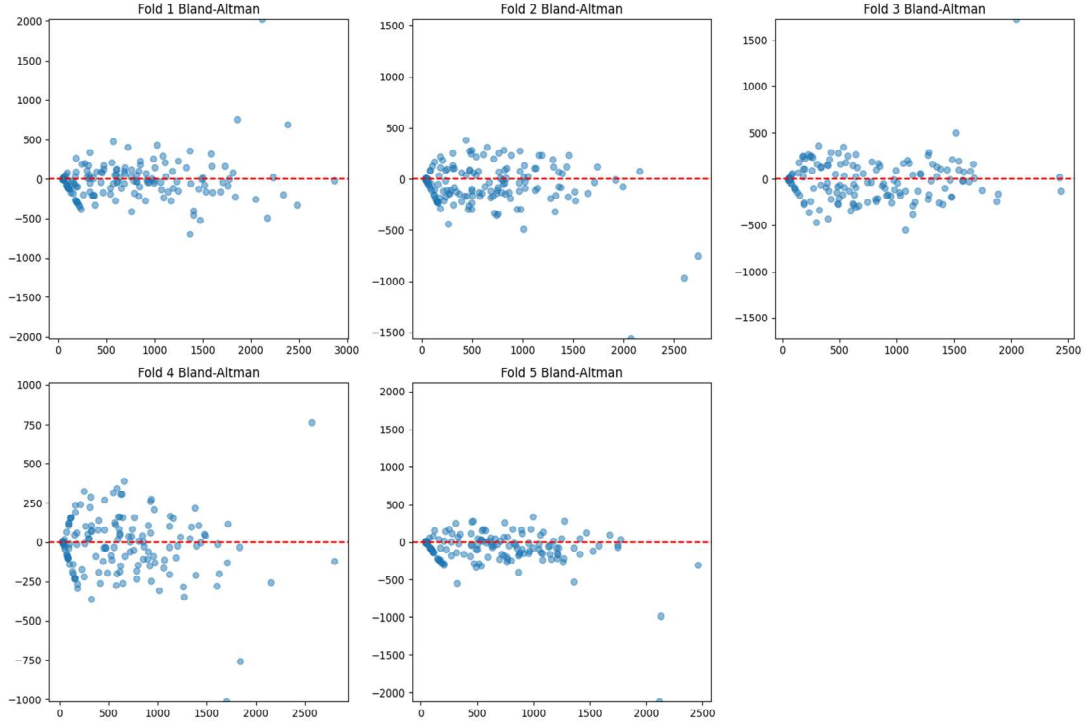


Fig. 5. Bland-Altman analysis for cTMTV and gtTMTV in the lymphoma patients of the test set of each fold, and these analyses were performed using the five-fold cross-validation method.

Linear regression analysis showed an average R^2 of 0.858, with the highest R^2 of 0.89 in the fourth fold. This demonstrates consistency between the cTMTV and gtTMTV. Pairwise t-tests revealed statistically significant differences between cTMTV and gtTMTV, highlighting the model's precision. Additionally, Pearson correlation analysis yielded a coefficient of 0.92 ($p < 0.05$), further indicating a strong correlation. Bland Altman analysis assessed the agreement between model calculations and actual measurements. Most comparisons were within acceptable limits, despite variability across folds.

4 Discussion

4.1 Ablation experiment

To evaluate the impact of different modules in the proposed method, we conducted a series of ablation experiments to scrutinize the effects of each module.

Base Model: Compared to the proposed model, the Base Model features a single encoder that utilizes convolutional block instead of the ViT structure in the end of the encoder. In the decoder, the reconstruction blocks receive the intermediate feature from encoder and the output of the last reconstruction block.

Trans Encoder Model (TEM): Base on the Base Model, TEM is a single-modality network, which replaces the deepest convolutional block to a ViT structure.

Double Encoder Model (DEM): DEM extends the Base Model by adding a CT modality branch in the encoder, forming a double encoder structure. Multimodal feature fusion is achieved through concatenation and convolution operations. The reconstruction blocks in the decoder receive the fused features and the output of the last reconstruction block.

Double Transformer Encoder Model (DTEM): Similar to DEM, DTEM employs a double encoder structure and integrates transformer by replacing the deepest convolutional block of each encoder with a ViT structure.

Double Encoder Cross Attention Fusion Model (DECAFm): Based on the DEM, DECAFm incorporates the MMCAF module for multimodal feature fusion. The reconstruction blocks in the decoder receive the fusion features from the MMCAF module and the output of the last reconstruction block.

Table 3: Result of Ablation Experiments. The bold texts indicate the highest achieved performance.

Model	Module	DSC	HD (mm)	Sensitivity	Specificity
Base Model	<input checked="" type="checkbox"/> PET <input type="checkbox"/> CT <input type="checkbox"/> MMCAF <input type="checkbox"/> ViT	0.8011±0.0472	3.13±1.37	0.8066±0.0749	0.9962±0.0012
Base Model	<input type="checkbox"/> PET <input checked="" type="checkbox"/> CT <input type="checkbox"/> MMCAF <input type="checkbox"/> ViT	0.1651±0.1253	26.61±8.56	0.5728±0.1394	0.9612±0.0094
DEM	<input checked="" type="checkbox"/> PET <input checked="" type="checkbox"/> CT <input type="checkbox"/> MMCAF <input type="checkbox"/> ViT	0.8147±0.0216	3.06±1.37	0.8053±0.0385	0.9954±0.0005
DECAFm	<input checked="" type="checkbox"/> PET <input checked="" type="checkbox"/> CT <input checked="" type="checkbox"/> MMCAF <input type="checkbox"/> ViT	0.8268±0.0265	2.92±0.82	0.8185±0.0049	0.9968±0.0024
TEM	<input checked="" type="checkbox"/> PET <input type="checkbox"/> CT <input type="checkbox"/> MMCAF <input checked="" type="checkbox"/> ViT	0.8723±0.0133	2.83±0.71	0.8861±0.0232	0.9973±0.0011
TEM	<input type="checkbox"/> PET <input checked="" type="checkbox"/> CT <input type="checkbox"/> MMCAF <input checked="" type="checkbox"/> ViT	0.2144±0.0875	18.84±6.21	0.6693±0.725	0.9883±0.0085
DTEM	<input checked="" type="checkbox"/> PET <input checked="" type="checkbox"/> CT <input type="checkbox"/> MMCAF <input checked="" type="checkbox"/> ViT	0.8845±0.0140	2.79±0.21	0.8892±0.0674	0.9923±0.0020
Ours	<input checked="" type="checkbox"/> PET <input checked="" type="checkbox"/> CT <input checked="" type="checkbox"/> MMCAF <input checked="" type="checkbox"/> ViT	0.9173±0.0071	2.71±0.25	0.9462±0.0223	0.9986±0.0008

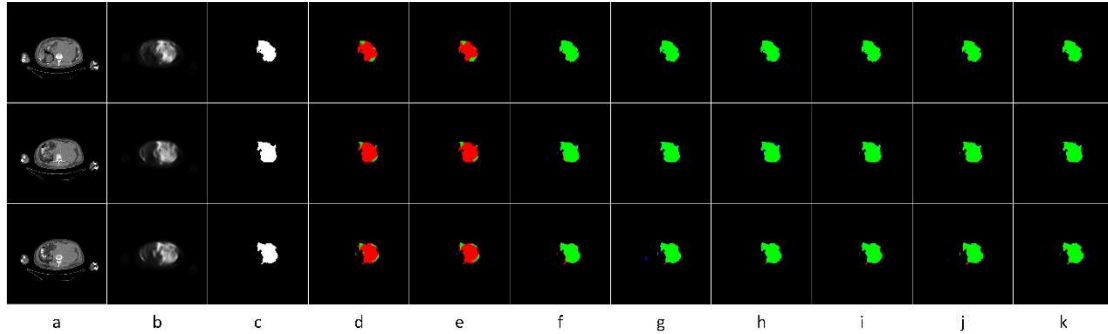


Fig. 6. Difference maps of ablation experiments. The green, red, and blue regions represent true positive, false negative, and false positive pixels, respectively. (a). CT images, (b). PET images, (c). ground truth. Difference maps generated by (d). Base Model with CT, (e). TEM with CT, (f). Base Model with PET, (g). DEM, (h). DECAFm, (i). TEM with PET, (j). DTEM, (k). our method.

As demonstrated in Table 2, the DEM with PET and CT branches achieved a DSC increase from 0.8011 to 0.8147 compared to the Base Model with PET only. This indicates that the addition of CT data is beneficial for lymphoma segmentation. Furthermore, the DSC of the Base Model using only CT data is 0.16, emphasizing the indispensable role of PET in lymphoma segmentation task. Figure 6 illustrates that detecting lymphoma tissue in CT is challenging, while the details of the tissue are clearly visible in PET. In the multimodal methods, incorporating MMCAF proves superior to using concatenation and convolution methods, highlighting the advantage of the cross-attention mechanism. MMCAF effectively utilizes the complementary information of multimodal data. It is noteworthy that the introduction of the vision transformer

module yields a significant performance improvement. For example, in DEM and DTEM (with the transformer), the averaged DSC was increased from 0.8147 to 0.8845, demonstrating a substantial improvement and the significance of applying the vision transformer in medical image processing.

4.2 Comparison with other studies

Many existing studies proposed automatic segmentation of lymphoma using private datasets. Li et al.¹² proposed an end-to-end network structure for lymphoma segmentation, focusing on semi-supervised lymphoma segmentation. Their model was trained and tested on PET/CT data from 80 lymphoma cases, including 35 annotated cases and 45 unannotated cases, and achieved a DSC of 0.72. Yuan et al.¹⁵ proposed a dual encoders network for lymphoma segmentation, achieving a DSC of 0.73 in a dataset of 45 DLBCL patients. In a study by Blanc-Durand et al.⁷, PET/CT data from 639 DLBCL patients were used for training and validation, and then 94 cases were used for testing. They employed a 3D U-Net network and achieved a DSC of 0.73. Huang et al.¹⁴ proposed a segmentation method using uncertainty quantification and deep learning. They trained and tested their model on PET/CT scans from 173 DLBCL patients, achieving a DSC of 0.84. It is worth noting that, except for Yuan et al.¹⁵, other studies did not use a dual encoder structure. Moreover, none of them incorporated a transformer for lymphoma segmentation. Our method achieved a DSC of 0.9173, which outperformed these studies significantly. As shown in Table 2, the vision transformer, coupled with dual encoders fusing PET and CT data via the MMCAF module, notably improved the segmentation performance.

4.3 TMTV calculation

TMTV holds paramount importance in the management and treatment planning for lymphoma patients. Clinically, TMTV is frequently employed to evaluate disease prognosis and treatment response. The results indicate a high level of consistency in the performance of the segmentation model across different datasets within a five-fold cross-validation framework. This consistency underscores the model's reliability in predicting TMTV across various clinical scenarios. Notably, in the fourth fold, the R^2 value for TMTV calculation reached 0.8892, marking the most remarkable performance. This suggests that the data distribution in this fold closely aligns with the model's training data, leading to increased accuracy in TMTV prediction.

4.4 Limitations

Although our lymphoma segmentation approach yields accurate results, it comes with a high computational requirement. In addition, since the PET and CT data were not acquired simultaneously, slight patient displacement in the PET/CT scanner would lead to the challenge of data feature mismatch. Despite our use of rigid registration for data alignment, its accuracy may be influenced.

5 Conclusion

In this study, we proposed a network for the automatic segmentation of DLBCL lesions in PET/CT images. Our model outperformed existing methods in both DLBCL lesion segmentation and TMTV calculation. This study contributes a powerful tool for the diagnosis and treatment of lymphoma patients. Our future work will focus on reducing the computational complexity, expanding the dataset size, and improving the practical applicability of our method.

Funding: This study received support from National Natural Science Foundation of China (Grant Numbers: 62106233, 62303427, and 82370513), Young Teacher Foundation of Henan Province (Grant No.2021GGJS093), Henan Science and Technology Development Plan (Grant Number: 232102210010, 232102210062, and 222102210219) and Peking University Baidu Fund [2020BD038].

References

1. Jhanwar YS, Straus DJ. The role of PET in lymphoma. *Journal of Nuclear Medicine*. 2006;47(8):1326-1334.
2. Jiang C, Teng Y, Zheng Z, Zhou Z, Xu J. Value of total lesion glycolysis and cell-of-origin subtypes for prognostic stratification of diffuse large B-cell lymphoma patients. *Quantitative imaging in medicine and surgery*. 11(6):2509-2520.
3. Nestle U, Schaefer-Schuler A, Kremp S, Groeschel A, Kirsch CM. Target volume definition for 18F-FDG PET-positive lymph nodes in radiotherapy of patients with non-small cell lung cancer. *European Journal of Nuclear Medicine & Molecular Imaging*. 2007;34(4):453-462.
4. Li H, Jiang H, Li S, Wang M, Wang Y. DenseX-Net: An End-to-End Model for Lymphoma Segmentation in Whole-body PET/CT Images. *IEEE Access*. 2019;PP(99):1-1.
5. Boellaard R, Delgado-Bolton R, Oyen WJ, et al. FDG PET/CT: EANM procedure guidelines for tumour imaging: version 2.0. *European journal of nuclear medicine and molecular imaging*. 2015;42:328-354.
6. Jiang C, Chen K, Teng Y, et al. Deep learning-based tumour segmentation and total metabolic tumour volume prediction in the prognosis of diffuse large B-cell lymphoma patients in 3D FDG-PET images. *European Radiology*. 2022;32(7):4801-4812.
7. Blanc-Durand P, Jégou S, Kanoun S, et al. Fully automatic segmentation of diffuse large B cell lymphoma lesions on 3D FDG-PET/CT for total metabolic tumour volume prediction using a convolutional neural network. *European Journal of Nuclear Medicine and Molecular Imaging*. 2021;48:1362-1370.
8. Chen J, Lu Y, Yu Q, et al. Transunet: Transformers make strong encoders for medical image segmentation. *arXiv preprint arXiv:210204306*. 2021;
9. Li K, Zhang R, Cai W. Deep learning convolutional neural network (DLCNN): unleashing the potential of 18F-FDG PET/CT in lymphoma. *American Journal of Nuclear Medicine and Molecular Imaging*. 2021;11(4):327.
10. Hellwig D, Graeter TP, Ukena D, et al. 18F-FDG PET for mediastinal staging of lung cancer: which SUV threshold makes sense? *Journal of Nuclear Medicine*. 2007;48(11):1761-1766.
11. Hatt M, Lee JA, Schmidtlein CR, et al. Classification and evaluation strategies of auto - segmentation approaches for PET: Report of AAPM task group No. 211. *Medical physics*. 2017;44(6):e1-e42.
12. Li H, Jiang H, Li S, et al. DenseX-net: an end-to-end model for lymphoma segmentation in whole-body PET/CT images. *Ieee Access*. 2019;8:8004-8018.
13. Huang L, Denœux T, Tonnelet D, Decazes P, Ruan S. Deep PET/CT fusion with Dempster-Shafer theory for lymphoma segmentation. *Springer*; 2021:30-39.
14. Huang L, Ruan S, Decazes P, Denœux T. Lymphoma segmentation from 3D PET-CT images using a deep evidential network. *International Journal of Approximate Reasoning*. 2022;149:39-60.
15. Yuan C, Zhang M, Huang X, et al. Diffuse large B - cell lymphoma segmentation in PET - CT images via hybrid learning for feature fusion. *Medical Physics*.

2021;48(7):3665-3678.

16. Luo W, Li Y, Urtasun R, Zemel R. Understanding the effective receptive field in deep convolutional neural networks. *Advances in neural information processing systems*. 2016;29

17. Jacobsen J-H, Van Gemert J, Lou Z, Smeulders AW. Structured receptive fields in cnns. 2016:2610-2619.

18. Bi J, Zhu Z, Meng Q. Transformer in computer vision. *IEEE*; 2021:178-188.

19. Parvaiz A, Khalid MA, Zafar R, Ameer H, Ali M, Fraz MM. Vision Transformers in medical computer vision—A contemplative retrospection. *Engineering Applications of Artificial Intelligence*. 2023;122:106126.

20. Zhong Z, Kim Y, Plichta K, et al. Simultaneous cosegmentation of tumors in PET - CT images using deep fully convolutional networks. *Medical physics*. 2019;46(2):619-633.

21. Zhao X, Li L, Lu W, Tan S. Tumor co-segmentation in PET/CT using multi-modality fully convolutional neural network. *Physics in Medicine & Biology*. 2018;64(1):015011.

22. Zhou Z, Jain P, Lu Y, et al. Computer-aided detection of mantle cell lymphoma on 18F-FDG PET/CT using a deep learning convolutional neural network. *American Journal of Nuclear Medicine and Molecular Imaging*. 2021;11(4):260.

23. Albano D, Bertoli M, Battistotti M, et al. Prognostic role of pretreatment 18F-FDG PET/CT in primary brain lymphoma. *Annals of nuclear medicine*. 2018;32:532-541.

24. Thie JA. Understanding the standardized uptake value, its methods, and implications for usage. *Journal of Nuclear Medicine*. 2004;45(9):1431-1434.

25. He K, Zhang X, Ren S, Sun J. Deep residual learning for image recognition. 2016:770-778.

26. Dosovitskiy A, Beyer L, Kolesnikov A, et al. An image is worth 16x16 words: Transformers for image recognition at scale. *arXiv preprint arXiv:201011929*. 2020;

27. Vaswani A, Shazeer N, Parmar N, et al. Attention is all you need. *Advances in neural information processing systems*. 2017;30

28. Stevens E, Antiga L, Viehmann T. *Deep learning with PyTorch*. Manning Publications; 2020.

29. Kingma DP, Ba J. Adam: A method for stochastic optimization. *arXiv preprint arXiv:14126980*. 2014;

30. Ronneberger O, Fischer P, Brox T. U-net: Convolutional networks for biomedical image segmentation. *Springer*; 2015:234-241.

31. Martín-Saladich Q, Reynés-Llompart G, Sabaté-Llobera A, Palomar-Muñoz A, Domingo-Domènech E, Cortés-Romera M. Comparison of different automatic methods for the delineation of the total metabolic tumor volume in I–II stage Hodgkin Lymphoma. *Scientific Reports*. 2020;10(1):12590.